

The exclusive surface and electronic effects of Ni on promoting the activity of Pt towards alkaline hydrogen oxidation

Kuncan Wang^{1,§}, Hao Yang^{2,§}, Juntao Zhang¹, Guomian Ren³, Tao Cheng², Yong Xu³ (✉), and Xiaoqing Huang¹ (✉)

¹ State Key Laboratory of Physical Chemistry of Solid Surfaces, College of Chemistry and Chemical Engineering, Xiamen University, Xiamen 361005, China

² Institute of Functional Nano & Soft Materials (FUNSOM), Jiangsu Key Laboratory for Carbon-Based Functional Materials & Devices, Soochow University, Suzhou 215123, China

³ Guangzhou Key Laboratory of Low-Dimensional Materials and Energy Storage Devices, Collaborative Innovation Center of Advanced Energy Materials, School of Materials and Energy, Guangdong University of Technology, Guangzhou 510006, China

[§] Kuncan Wang and Hao Yang contributed equally to this work.

© Tsinghua University Press 2022

Received: 6 January 2022 / Revised: 10 February 2022 / Accepted: 11 February 2022

ABSTRACT

Ni modification is considered as an efficient strategy for boosting the performance of Pt towards alkaline hydrogen oxidation reaction (HOR), yet its specific role is largely undecoded. Here, ultrathin Pt nanowires (NWs) are selected as models for revealing the significance of Ni modification on HOR by precisely positioning Ni on distinct positions of Pt NWs. Ni solely influences the electronic properties of Pt and thus weakens 'H adsorption when it is located in the core of PtNi alloyed NWs, leading to a moderate improvement of alkaline HOR activity. When Ni is distributed in both core and surface of PtNi alloyed NWs, Ni strongly weakens 'H adsorption but strengthens 'OH adsorption. On the other hand, the electronic properties of Pt are hardly influenced when Ni is deposited on the surface of Pt NWs, on which the strong 'H and 'OH adsorptions lead to the improved HOR activity. This work reveals the significance of Ni modification on HOR, but also promotes the fundamental researches on catalyst design for fuel cell reactions and beyond.

KEYWORDS

ultrathin Pt nanowire, surface decoration, Ni location, electronic property, hydrogen oxidation reaction

1 Introduction

Energy crisis and environmental protection are among the most important issues in the world [1, 2]. Under such circumstances, hydrogen (H₂) has been regarded as an ideal energy carrier, and hydrogen fuel cells (HFCs) have attracted increasing attention in recent years [3, 4]. As the anode reaction, hydrogen oxidation reaction (HOR) plays a vital role in improving the efficiency of HFCs. Generally, Pt has been widely used as the catalyst for HOR. However, Pt suffers from the drawback of slow HOR kinetics in alkaline conditions, where the alkaline kinetics is about two orders of magnitude lower than that in acidic conditions. Therefore, it is highly desired to develop efficient Pt-based catalysts for alkaline HOR [5].

Over the past decades, great efforts have been devoted to the modifications of Pt for improving its alkaline HOR performance [6–10]. Various promoters are employed to composite with Pt for alkaline HOR. In particular, Ni has been widely used to composite with Pt for enhancing its alkaline HOR activity. For instance, Strmcnik et al. proposed that the modification of Pt with Ni can facilitate 'OH adsorption and thus significantly enhanced alkaline HOR [2]. Wang and co-workers demonstrated that Ni alloyed with Pt can strongly improve the alkaline HOR activity by

promoting 'OH adsorption [11]. On the other hand, it has been reported that the alloying of Ni with Pt may mainly influence the electronic properties other than facilitating the 'OH adsorption [11, 12]. Despite substantial attentions have been devoted to the Pt modification with Ni, the specific role of Ni is largely undecoded yet, which severely impedes the rational design of more efficient catalysts for alkaline HOR.

In this work, we have devoted our efforts to exploring the specific function of Ni on alkaline HOR by precisely modifying ultrathin Pt NWs with Ni. When Ni is located in the core of PtNi alloyed ultrathin NWs (named as PtNi-C), Ni solely influences the electronic properties of Pt and thus weakens the adsorption of 'H, leading to a moderate improvement of alkaline HOR activity. When Ni is evenly distributed in both core and surface of PtNi alloyed ultrathin NWs (named as PtNi-A), PtNi-A exhibits weaker 'H adsorption but stronger 'OH adsorption compared with PtNi-C, leading to the improved alkaline HOR performance. On the other hand, when Ni is located on the surface of Pt ultrathin NWs (named as PtNi-S), on which the electronic properties of Pt are hardly influenced by the surface Ni, PtNi-S displays strong adsorptions for both 'H and 'OH, resulting in the significantly improved HOR activity. Experimental and theoretical studies show that the surface Ni deposition on Pt NWs surface can

Address correspondence to Yong Xu, yongxu@gdut.edu.cn; Xiaoqing Huang, hxq006@xmu.edu.cn



regulate the adsorption towards 'OH, while the alloyed Ni with Pt NWs strongly varies the electronic properties of Pt and thus strongly weakens the adsorption towards 'H. This work not only clearly reveals the specific role of Ni on ultrathin Pt NWs for alkaline HOR, but also promotes the catalyst design for fuel cell reactions.

2 Experimental section

2.1 Chemicals

Platinum(II) acetylacetonate ($\text{Pt}(\text{acac})_2$, 97%) was purchased from Sigma-Aldrich. Nickel(II) acetylacetonate ($\text{Ni}(\text{acac})_2$, 95%) and oleylamine (OAm, 80–90%) were obtained from Aladdin-reagent Inc. (Shanghai, China). Molybdenum carbonyl ($\text{Mo}(\text{CO})_6$, 98%) was obtained from Strem Chemicals Inc. Glucose ($\text{C}_6\text{H}_{12}\text{O}_6$, > 99.7% (AR)), hexadecyltrimethylammonium chloride (CTAC, > 98.0% (CP)), cyclohexane (C_6H_{12} , > 99.7% (AR)), potassium hydroxide (KOH, > 85.0% (AR)), ethanol ($\text{C}_2\text{H}_5\text{OH}$, > 99.7% (AR)), isopropanol ($\text{C}_3\text{H}_8\text{O}$, > 99.7% (AR)) and acetic acid (CH_3COOH , > 99.5% (AR)) were all purchased from Sinopharm Chemical Reagent Co., Ltd. (Shanghai, China). Perchloric acid (HClO_4 , 70%–72% (AR)) was obtained from Tianjin Zhengcheng Chemical Co., Ltd. (China). Nafion (perfluorosulfonic acid-PTFT copolymer, 5% w/w solution) came from Alfa Aesar. Commercial Pt/C (20 wt.% Pt on Vulcan XC72R carbon) was provided by JM. α -Aluminum oxide ($\alpha\text{-Al}_2\text{O}_3$, > 99%, diameter: 50 nm) was purchased from Tianjin Aida Hengsheng Technology Co., Ltd. All the chemicals were used as received without further purification. The water ($18\text{ M}\Omega\cdot\text{cm}^{-1}$) used in all experiments was prepared by passing through an ultra-pure purification system (Aqua Solutions).

2.2 Fabrication of samples

Synthesis of Pt NWs and PtNi-S. In a typical synthesis of Pt NWs, $\text{Pt}(\text{acac})_2$ (10 mg), $\text{Mo}(\text{CO})_6$ (30 mg), and CTAC (55 mg) were dispersed in OAm (5 mL) in a glass vial (volume: 30 mL) with ultrasonication for 2 h (the glass vial was kept sealed) to generate a homogeneous mixture. The obtained mixture was then heated from room temperature to 160 °C and held at 160 °C for 2 h in an oil bath. Upon the resulting mixture (black) being cooled to room temperature, the products were collected by centrifugation and washed with a cyclohexane/ethanol (1:8, v/v) mixture for three times. A two-step method was adopted for the synthesis of PtNi-S. Specifically, a certain amount of $\text{Ni}(\text{acac})_2$ (3, 5, or 7 mg) was added into the collected Pt NWs and then underwent the sequential treatments of ultrasonication, heating, cooling, centrifugation, and washing, which were the same with the synthesis of Pt NWs.

Synthesis of PtNi-A and PtNi-C. The synthetic process of PtNi-A is similar to that for Pt NWs except for adding $\text{C}_6\text{H}_{12}\text{O}_6$ (60 mg) and $\text{Ni}(\text{acac})_2$ (5, 7 or 9 mg). PtNi-C was prepared by etching the surface Ni of PtNi-A. Specifically, PtNi-A was mixed with acetic acid (10 mL) and then stirred at 100 °C for 2.5 h. Finally, the product was collected by centrifugation and washed with ethanol for three times.

Preparation of supported catalysts. Prior to catalytic evaluation, the obtained samples were supported on the commercial carbon (C, Vulcan). In particular, the collected NWs were dispersed in cyclohexane, followed by adding C support under sonication for 1 h (Pt loading: ~ 20 wt.%). Afterwards, the obtained mixture was collected by centrifugation and washed with acetic acid/ethanol (1:8, v/v) for two times and further washed with ethanol for another three times. After drying at 80 °C, the catalysts were finally calcined at 200 °C with a heating rate of $5\text{ }^\circ\text{C}\cdot\text{min}^{-1}$ in air for 2 h.

2.3 Characterizations

Powder X-ray diffraction (XRD) patterns were collected on a X' Pert Pro X-ray diffractometer (PANalytical BV, Netherlands) with a $\text{Cu K}\alpha$ X-ray source ($\lambda = 1.540598\text{ \AA}$), and operated at 40 kV and 30 mA with a step size of 0.02° . The morphology was observed by using a JEOL 1400 TEM (Japan) operating at 100 kV accelerating voltage. Transmission electron microscopy (TEM) images, high-resolution TEM (HRTEM) images, and high-angle annular dark-field scanning TEM (HAADF-STEM) images of the products were obtained by a Tecnai F30 microscope (TECNAI F30, USA) operating at 300 kV. Elemental mapping was collected by energy-dispersive X-ray spectroscopy (EDS, TECNAI F30, USA). The composition of the catalysts was obtained by using a scanning electron microscopy–energy-dispersive spectroscopy (SEM-EDS) system (ZEISS SIGMA, Germany). X-ray photoelectron spectroscopy (XPS) was conducted on a Thermo Fisher Scientific diffractometer using $\text{Al K}\alpha$ (1486.6 eV) radiation as an X-ray source in which the binding energy was calibrated with C 1s 284.8 eV. Pt and Ni amounts were determined by inductively coupled plasma optical emission spectrometry (ICP-OES, iCAP 7000 SERIES). High-sensitivity low-energy ion scattering spectroscopy (HS-LEISS) characterizations were carried out with an ION-TOF Qtac100 instrument. Neon was selected as the ion source with a kinetic energy of 5 keV. The ion flux is $1600\text{ pA}\cdot\text{m}^{-1}$ and the spot size is $2\text{ mm} \times 2\text{ mm}$. Temperature-programmed desorption of H_2 (H_2 -TPD) experiments were performed on an AutoChem II 2920 (Micromeritics) apparatus with a mass spectrometer (MS) detector. 30 mg sample was pretreated at 200 °C in Ar (99.99%, $30\text{ mL}\cdot\text{min}^{-1}$) and then cooled down to 50 °C. Afterwards, H_2 (99.99%, $30\text{ mL}\cdot\text{min}^{-1}$) was introduced for 30 min and then flushed with Ar (99.99%, $30\text{ mL}\cdot\text{min}^{-1}$) for 2 h. Finally, the temperature was increased from 50 to 900 °C with a heating rate of $10\text{ }^\circ\text{C}\cdot\text{min}^{-1}$ for desorption. *In situ* diffuse reflectance infrared Fourier transform spectroscopy (DRIFTS) of H_2O adsorption was performed on an Fourier-transform infrared (FTIR) spectrometer (Thermo, Nicolet iS50). Prior to DRIFTS test, the sample was pretreated in N_2 (99.99%, $30\text{ mL}\cdot\text{min}^{-1}$) at 200 °C for 30 min. After cooling to 80 °C, the background spectra were recorded. H_2O was introduced onto the catalyst by N_2 (99.99%, $30\text{ mL}\cdot\text{min}^{-1}$) for 1 h. Afterwards, the surface of sample was flushed with N_2 (99.99%, $30\text{ mL}\cdot\text{min}^{-1}$) at 80 °C for another 30 min.

2.4 Simulation details

The *ab initio* quantum mechanical calculations were performed using Vienna *Ab initio* Simulation Package (VASP) at a version of 5.4.4 with the projector augmented wave (PAW) method and a plane wave basis set [13–16]. The method is density functional theory (DFT) with generalized gradient approximations (GGA) of Perdew-Burke-Ernzerhof (PBE) functional [17, 18]. A dispersion correction, DFT-D3 method with Becke-Jonson damping [19], was included in the calculations. The energy-cut-off was set to 400 eV. Spin polarization doesn't have an appreciable influence on the overall energies and therefore has not been included in calculations. The electronic self-consistent step is considered to be converged when the changes of total energy and eigenvalues between two steps are both smaller than 10^{-6} eV . The partial occupancies for each orbital were set with First order Methfessel-Paxton scheme in the smearing width of the 0.2 eV. The dipole moment corrections for the total energy were considered in the direction normal to the surface. A conjugate-gradient algorithm was used to relax the ions in energy minimization. The minimization was considered to be converged when all the forces were smaller than $10^{-2}\text{ eV}\cdot\text{\AA}^{-1}$. The implicit solvation model of

VASP sol was employed to describe the effect of electrostatics, cavitation, and dispersion on the interaction between a solute and solvent [20, 21]. The relative permittivity of the solvent is 78.4, and the Debye screening length is 3.0 Å. The number of electrons in the simulations was tuned to match the target chemical potential of electron.

2.5 Electrochemical measurements by RDE

The electrocatalytic properties toward HOR were conducted by a rotating disc electrode (RDE) with a CHI 760E electrochemical workstation (Shanghai Chenhua Co.). A three-electrode cell was used, in which 0.1 M KOH solution served as the electrolyte, a saturated calomel electrode (SCE) as the reference electrode, a graphite rod as the counter electrode, and a glassy carbon electrode (GCE, diameter: 5 mm and area: 0.196 cm²) as the working electrode, respectively. In each test, 2 mg catalyst was dispersed in a mixture containing isopropanol (990 µL) and 0.5 wt.% Nafion solution (10 µL) with ultrasonication for 30 min to prepare a 2 mg·mL⁻¹ catalyst ink. Then, 5 µL ink was cast on the GCE (polished by α-Al₂O₃) and allowed to dry to form a catalyst thin film (the final Pt loading was 10 µg·cm⁻²). All electrolytes were bubbled with H₂ throughout the whole electrochemical experiments, and the HOR polarization curves were recorded at a scan rate of 10 mV·s⁻¹. The rotating speed of the electrode was set at 1,600 rpm. The recorded potentials were referred to reversible hydrogen electrode (RHE) with iR-correction.

To calculate the electrochemical surface area (ECSA), the cyclic voltammogram (CV) test was performed for each sample in 0.1 mol·L⁻¹ HClO₄ at room temperature, and the potential was set from 0.05 to 1.2 V vs. RHE at a scanning rate of 50 mV·s⁻¹. The ECSA of each sample was determined by using the hydrogen desorption charges (between 0.05 and 0.4 V vs. RHE) from the obtained stable CV curve (after 100 potential cycles), as we previously reported [22].

3 Results and discussion

Ultrathin Pt NWs were fabricated via a wet chemistry technique by adding Pt(acac)₃, Mo(CO)₆, and CTAC into OAm [23]. After ultrasonication, the obtained mixture was then heated from room temperature to 160 °C and held for 2 h in an oil bath. Upon the resulting black mixture being naturally cooled to room temperature, the products were collected by centrifugation and washed with a cyclohexane/ethanol (1:8, v/v) mixture for three times. The synthetic process of ultrathin PtNi-A NWs is similar to that of Pt NWs except for introducing additional Ni(acac)₂ and C₆H₁₂O₆. The PtNi-S was fabricated by decorating Ni(acac)₂ onto the as-prepared Pt NWs, and the PtNi-C was obtained by etching PtNi-A NWs with by etching PtNi-A NWs with acetic acid (Fig. 1(a)).

TEM images show that the diameter of Pt NWs is ~ 2.1 nm (Fig. 1(b)), and the lattice distance of 0.227 nm is ascribed to Pt(111) facet (the insert in Fig. 1(b)). When Ni is deposited on Pt NWs (PtNi-S), the mean diameter and the lattice distance of PtNi-S NWs are very similar to those of pure Pt NWs (Fig. 1(c) and the insert), suggesting that the location of Ni on the surface of PtNi-S displays negligible effect on the structure of Pt NWs. For PtNi-A, no obvious changes in the morphology and diameter are observed after alloying Ni with Pt NWs (Fig. 1(d)), and the slight lattice contraction (0.221 nm) can be attributed to the introduction of Ni (the insert in Fig. 1(d)). After etching PtNi-A NWs with acetic acid, the morphology and the lattice distance of PtNi-S are largely maintained (Fig. 1(e)), suggesting that acetic acid only etches the surface Ni atoms. Moreover, XRD was carried out to determine the structures of Pt NWs, PtNi-S, PtNi-A, and PtNi-C. As shown in Fig. 1(f), the peaks at 39.5°, 46.3°, and 67.5° in the XRD pattern of Pt NWs are ascribed to Pt(111), (200), and (220) facets, respectively. After decorating Pt NWs with Ni, the absence of Ni peaks is attributed to the high dispersity of Ni on the surface of PtNi-S. It is found that the peaks in the XRD patterns remain at the same positions when the amount of Ni(acac)₂ precursor is

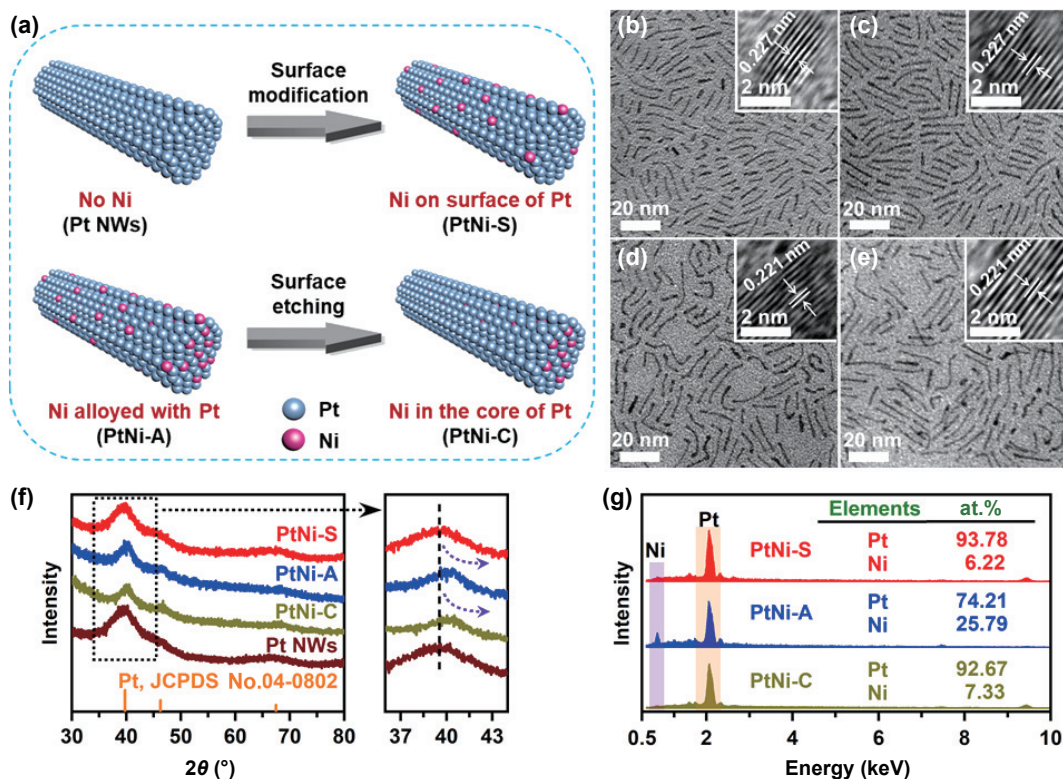


Figure 1 (a) Schematic illustration of Ni distributed on Pt NWs in distinct positions. TEM and HRTEM images of (b) Pt NWs, (c) PtNi-S, (d) PtNi-A, and (e) PtNi-C. (f) XRD patterns, and (g) EDS spectra of different samples.

increased from 3 to 7 mg except for the appearance of peaks of Ni (PDF No.: 04-0850) (Fig. S1(a) in the Electronic Supplementary Material (ESM)), further suggesting that the decoration of Ni atoms on the surface of Pt NWs displays negligible influence on the structure of Pt. For PtNi-A, the peak of Pt(111) facet positively shifts by 0.7° compared to that of pure Pt NWs, which is attributed to the lattice contraction after Ni introduction. The lattice contraction caused by Ni atoms has been further validated by increasing the content of Ni in PtNi alloyed NWs (Fig. S1(b) in the ESM) [23]. After etching with acetic acid, the PtNi alloyed structure remains, suggesting that acetic acid only removes the surface Ni. Results from SEM-EDS show that the atomic ratios of Pt/Ni for PtNi-S, PtNi-A, and PtNi-C are 93.8/6.2, 74.2/25.8, and 92.7/7.3, respectively (Fig. 1(g)), which are consistent with the results from ICP-OES (Table S1 in the ESM).

The structures of various samples were further studied by XPS measurement. Figure 2(a) shows the high resolution Pt 4f core-level spectra of different samples. In the Pt 4f XPS spectrum of Pt NWs, two peaks at the binding energy of ~ 71.9 and ~ 75.2 eV are ascribed to the $4f_{7/2}$ and $4f_{5/2}$ peaks of Pt^0 [12, 24, 25]. Compared to Pt NWs, the Pt 4f peaks of PtNi-A and PtNi-C positively shift by 0.6 eV, which is attributed to the electron transfer from the Pt d-band to Ni [12, 26, 27]. Moreover, the peaks in the Pt 4f XPS spectra can be deconvoluted into two pairs of doublets (Fig. 2(a)). Two peaks at ~ 72.0 and 75.0 eV are ascribed to Pt^0 $4f_{7/2}$ and $4f_{5/2}$, while the peaks at ~ 73.0 and 77.4 eV correspond to Pt^{2+} $4f_{7/2}$ and $4f_{5/2}$, respectively [12, 28]. The ratios of Pt^0 are estimated to be 70.84%, 71.87%, 75.63%, and 73.62% for Pt NWs, PtNi-S, PtNi-A, and PtNi-C, respectively. When Ni atoms are deposited on the surface of Pt NWs (i.e., PtNi-S), the Pt 4f XPS spectrum displays very similar peak positions in comparison to that of Pt NWs, indicating that the surface properties of Pt atoms in PtNi-S are almost the same to those of Pt NWs. The high-resolution Ni 2p spectra were further collected (Fig. 2(b)). When Ni atoms are deposited on the surface (i.e., PtNi-S), weak peaks of Ni^{2+} are observed at 856.6 and 874.2 eV (red spectrum in Fig. 2(b)). For PtNi-A, the corresponding peaks of Ni^0 (853.2 and 870.2 eV), Ni^{2+} (856.6 and 874.2 eV), and the satellites of Ni^{2+} (861.8 and 880.6 eV) are observed in the Ni 2p XPS spectrum [29]. The peaks of Ni^0 and Ni^{2+} can hardly be observed in the XPS spectrum of

PtNi-C (brown spectrum in Fig. 2(b)), indicating that the surface Ni has been etched by acetic acid. HS-LEISS was employed to further determine the structures [30, 31]. For PtNi-S, both Ni and Pt are detected on the surface, while only Pt can be identified on its sub-surface, indicating that Ni atoms are located on the surface of PtNi-S (Fig. 2(c)). Ni and Pt present both on the surface and sub-surface for PtNi-A, while Ni is absent on the surface of PtNi-C, further confirming the highly distinct distributions of Ni (Fig. 2(c)).

Based on the above detailed analyses, PtNi NWs with distinct Ni distributions have been successfully constructed. To study the effects of Ni distributions on catalytic performance, Pt NWs, PtNi-A, PtNi-C, and PtNi-S were used as catalysts for alkaline HOR (Fig. S2 and Table S1 in the ESM). Prior to the HOR test, various samples were supported on carbon black (Fig. S3 in the ESM). To directly compare the HOR activity of various catalysts, the ECSAs of different samples were determined [22, 32]. The obtained CVs in $0.1 \text{ mol}\cdot\text{L}^{-1} \text{ HClO}_4$ are given in Fig. S4 in the ESM. The ECSAs for Pt/C JM, Pt NWs, PtNi-S, PtNi-A, and PtNi-C are 58.50, 86.73, 74.91, 72.94, and $60.15 \text{ m}^2\cdot\text{g}_{\text{Pt}}^{-1}$, respectively (Table S1 in the ESM). The ECSAs for PtNi-S, PtNi-A, and PtNi-C are lower than that of Pt NWs, which is attributed to the coverage of Pt by Ni [33]. It is found that Pt-based NWs exhibit superior activity to the commercial Pt/C (i.e., Pt/C JM), indicating this unique morphology of ultrathin NWs can facilitate the HOR activity [22, 34]. Moreover, PtNi-S with different contents of Ni on the surface (Fig. S5(a) in the ESM) and PtNi-A with different ratios of Pt and Ni were used as references for selecting the optimal compositions of Ni for HOR (Fig. S5(b) in the ESM). Afterwards, the linear sweep voltammetry (LSV) curves were collected by rotating disk electrode (RDE) in H_2 -saturated 0.1 M KOH (Fig. 3(a)). No current-voltage was observed for PtNi-S in N_2 -saturated 0.1 M KOH , while significant increases of voltages were observed for all catalysts when H_2 -saturated 0.1 M KOH were used, indicating the occurrence of HOR. It is noted that Pt NWs displays superior HOR activity to commercial Pt/C (Pt/C JM). After introducing Ni, the HOR activities are significantly improved. It is noted that PtNi-S displays the highest intrinsic HOR activity in comparison to PtNi-A and PtNi-C. Moreover, the HOR polarization curves of PtNi-S at different rotating speeds are given in Fig. 3(b). The

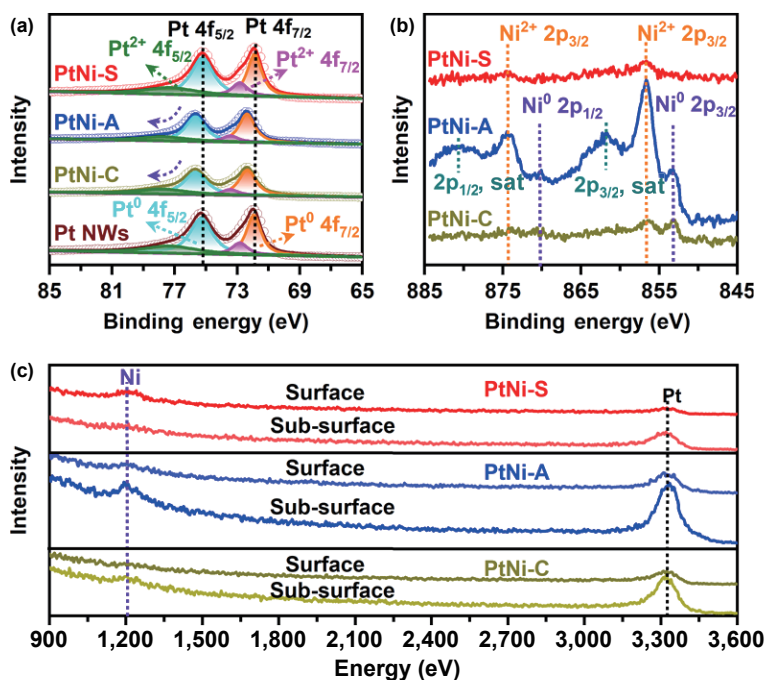


Figure 2 (a) Pt 4f XPS spectra, (b) Ni 2p XPS spectra, and (c) HS-LEISS for the surface species of different samples.

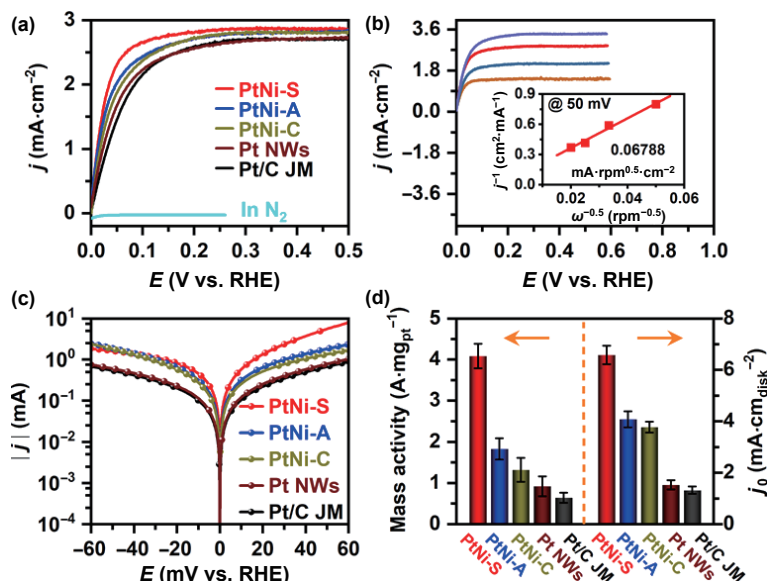


Figure 3 HOR performances of different catalysts. (a) HOR polarization curves, (b) HOR polarization curves of PtNi-S collected at different rotating speeds. Inset shows the Koutecky–Levich plot of PtNi-S at an overpotential of 50 mV. (c) HOR/hydrogen evolution reaction (HER) Tafel plots of different catalysts. (d) The corresponding histograms of the mass activities at 50 mV and the exchange current densities of different catalysts.

Koutecky–Levich plots of PtNi-S constructed at 50 mV exhibit a linear relationship between the inverse of overall current density (j) and the square root of the rotation rate (ω) (inset in Fig. 3(b)) [35, 36]. Consequently, the slope was calculated to be $0.0679 \text{ mA} \cdot \text{rpm}^{0.5} \cdot \text{cm}^{-2}$, which is close to the theoretical value ($0.0664 \text{ mA} \cdot \text{rpm}^{0.5} \cdot \text{cm}^{-2}$) for the $2e^-$ HOR process [37, 38]. By fitting the Butler–Volmer equation in the Tafel regions, the kinetic currents as a function of the overpotential for different catalysts were obtained [39]. As shown in Fig. 3(c), when the overpotential is 50 mV, the value of j_k decreases with the order of PtNi-S ($28.87 \text{ mA} \cdot \text{cm}_{\text{disk}}^{-2}$) > PtNi-A ($9.28 \text{ mA} \cdot \text{cm}_{\text{disk}}^{-2}$) > PtNi-C ($6.88 \text{ mA} \cdot \text{cm}_{\text{disk}}^{-2}$) > Pt NWs ($4.03 \text{ mA} \cdot \text{cm}_{\text{disk}}^{-2}$) > Pt/C JM ($3.42 \text{ mA} \cdot \text{cm}_{\text{disk}}^{-2}$). The exchange current density (j_0), a crucial indicator of HOR activity, was obtained by fitting the Butler–Volmer equation. It is found that PtNi-S exhibits an exchange current density of $6.58 \text{ mA} \cdot \text{cm}_{\text{disk}}^{-2}$ and mass activity of $4.08 \text{ A} \cdot \text{mg}_{\text{Pt}}^{-1}$, respectively, which are ~ 5.0 and ~ 6.3 times higher

than those of Pt/C JM (Fig. 3(d)). Additionally, PtNi-S catalyst was etched by acid under the same conditions with those for PtNi-C (termed as Acid PtNi-S). EDS results demonstrate that most of Ni are removed after such acid etching (Fig. S6(a) in the ESM). The obviously inferior HOR activity of Acid PtNi-S to PtNi-S suggests that the enhanced performance is strongly stemmed from the surface decorated Ni (Fig. S6(b) in the ESM). Given the highly Ni distribution-dependent HOR performance of PtNi-A, PtNi-C, and PtNi-S, more experiments were conducted to reveal the mechanism. We first evaluated the d-band centers (ϵ_d) for various catalysts. As shown in Fig. 4(a), the value of ϵ_d for PtNi-S is -3.56 eV , which is closer to the Fermi level compared to those of PtNi-A (-3.75 eV) and PtNi-C (-3.72 eV), indicating that the alloyed Ni with Pt (e.g., PtNi-A and PtNi-C) can strongly alter the electronic properties of Pt atoms and weaken the adsorption abilities towards reactants [24, 25, 37, 40]. Moreover, H_2 -TPD measurement was performed to evaluate the H_2 adsorption on

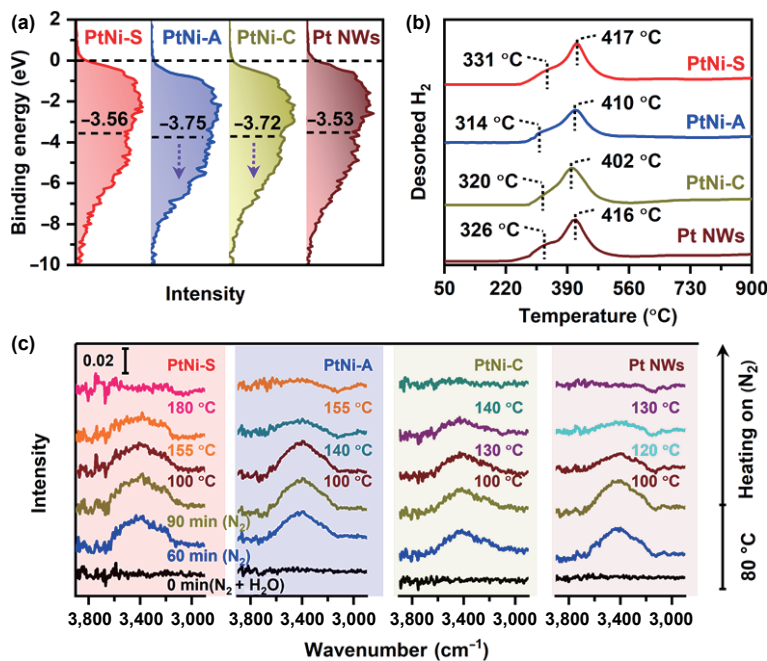


Figure 4 (a) Surface valence band photoemission spectra of different catalysts. (b) H_2 -TPD profiles and (c) *in situ* DRIFTS of H_2O adsorption of different catalysts.

catalyst. For PtNi-S, two peaks appear at ~ 331 and 417 °C in the H_2 -TPD curve, which are assigned to the strong adsorption of H_2 on Pt (Fig. 4(b)) [41]. Note that the peak positions of H_2 desorption in the H_2 -TPD curve of PtNi-S are close to those of Pt NWs, which suggests that the surface deposited Ni has negligible influence on H_2 adsorption on Pt. Compared to PtNi-A and PtNi-C, the H_2 desorption peaks for PtNi-S shift to higher temperature, indicating that PtNi-A and PtNi-C display weaker H_2 adsorption ability than PtNi-S, being consistent with d-band center analysis. Additionally, in situ DRIFTS was performed using H_2O as the probe to study the adsorption of OH on catalysts. Specifically, the catalysts were treated in N_2 at 200 °C for 30 min and then cooled to 80 °C. Prior to water introduction, no peaks are observed at the range of $3,000$ – $3,800$ cm^{-1} (black spectra in Fig. 4(c)), suggesting that the adsorbed H_2O on the surface of catalyst has been removed during pretreatment. After introducing water vapor by N_2 onto the catalysts, intense peaks appear at $\sim 3,400$ cm^{-1} in the DRIFTS spectra for all catalysts (blue spectra in Fig. 4(c)), which are ascribed to the characteristic peak of OH . Afterwards, the cell was flushed with N_2 for 30 min to remove the physically adsorbed H_2O (brown spectra in Fig. 4(c)). To evaluate the strength for OH adsorption, we gradually increased the temperature from 80 °C to 180 °C. It is found that the intensity of the peak at $\sim 3,400$ cm^{-1} gradually decreases with the increased temperature, which is attributed to the desorption of OH under high temperature. For PtNi-S, the peak completely disappears when the temperature is increased to 180 °C. In contrast, the temperatures of OH desorption for PtNi-A, PtNi-C and Pt NWs are 155 , 140 and 130 °C, respectively, indicating that PtNi-S displays much stronger adsorption to OH than PtNi-A, PtNi-C and Pt NWs. The above results imply that Pt species displays strong adsorption

to H , while the decoration of Ni on the surface (PtNi-S) can greatly facilitate the adsorption of OH , as a result of the significant enhancement on HOR activity.

To further understand the mechanism, DFT calculations were performed to simulate the elementary steps of HOR on PtNi-A, PtNi-C, and PtNi-S, respectively. As widely studied in previous reports, the hydrogen binding free energy (ΔG_{H^*}) and hydroxyl binding free energy (ΔG_{OH^*}), namely HBE and OHBE, are treated as the activity descriptor for HOR catalysis (Figs. S7 and S8 in the ESM). As shown in Fig. 5(a), the HBE of PtNi-S is -0.26 eV, which is much closer to the ideal value ($\Delta G_{\text{H}^*} = 0$) compared to PtNi-A and PtNi-C. For OHBE, PtNi-S displays the lowest free energy among these three catalysts, indicating its superior HOR activity to PtNi-A and PtNi-C (Fig. 5(b)). Moreover, we investigated the adsorption behaviors of H_2O (Fig. S9 in the ESM) as well as the H_2O formation (Fig. S10 in the ESM) from the surface adsorbed OH and H , which are the key step for HOR under alkaline conditions. As shown in Figs. 5(c) and 5(d), both the adsorption energy and formation energy of H_2O for PtNi-S are much higher than those of PtNi-A and PtNi-C, indicating that H_2O adsorption is thermodynamically favorable and therefore the kinetics on PtNi-S is significantly enhanced. Given the results from experiments, characterizations and DFT calculations, the functions of Ni are summarized in Fig. 5(e). In particular, pure Pt surface exhibits strong adsorption ability to H but weak adsorption to OH , and therefore displays low HOR activity in alkaline conditions. When Ni is deposited on the surface of Pt, for PtNi-S, the surface Ni exhibits weak influence to the electronic properties of Pt; that is, the H adsorption on Pt is hardly weakened. On the other hand, the surface Ni can significantly promote OH adsorption, leading to the enhanced HOR activity.

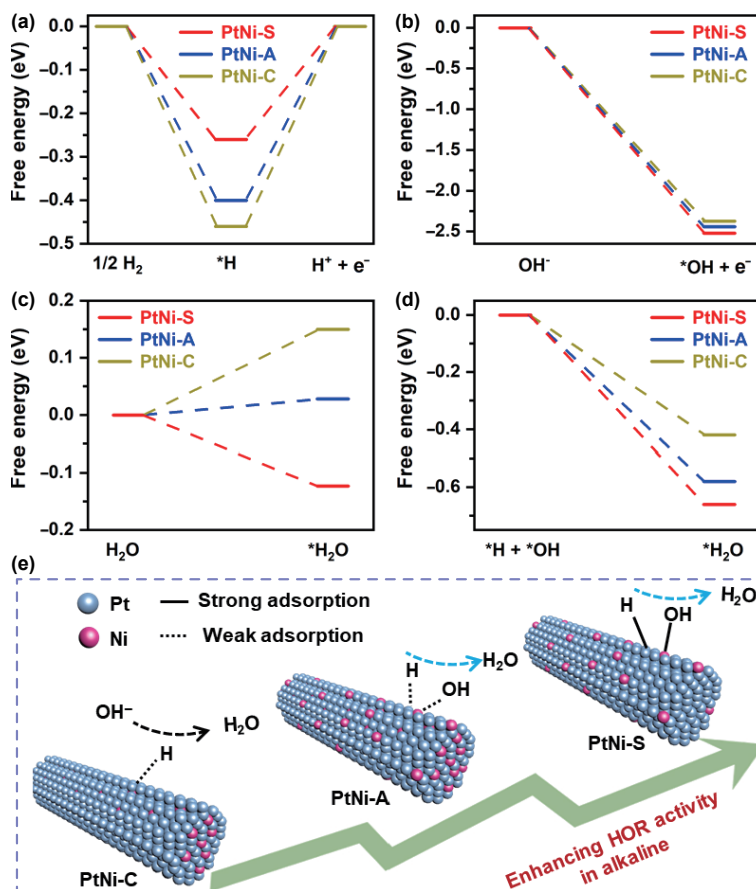


Figure 5 DFT simulations of the HOR processes on PtNi-S, PtNi-A and PtNi-C. (a) Gibbs free energy profiles for hydrogen adsorption (ΔG_{H^*}) and (b) Gibbs free energy profiles for hydroxyl adsorption (ΔG_{OH^*}). (c) Gibbs free energy profiles for water adsorption and (d) water formation. (e) Schematic illustration of the possible catalytic mechanism of different samples.

When Ni is located in the core position (e.g., PtNi-C), the surface electronic properties of Pt are altered, leading to the weakened 'H adsorption. Nevertheless, the absence of Ni on the surface will lead to the weak 'OH adsorption and thus inferior HOR activity to PtNi-S. When Ni is evenly alloyed with Pt (e.g., PtNi-C), despite the enhanced 'OH adsorption due to presence of Ni, the electronic properties of Pt is strongly altered, that is, the 'H adsorption is strongly weakened, leading to the superior HOR activity to PtNi-C but inferior HOR activity to PtNi-S.

4 Conclusions

In summary, we have clearly revealed the role of Ni on HOR activity by precisely controlling the structures of PtNi ultrathin NWs. The electronic properties and surface compositions can be systematically tuned by regulating the distributions of Ni on PtNi ultrathin NWs. In particular, alloying Pt with Ni can significantly alter the electronic properties of Pt, that is, weaken the adsorption ability to 'H, while the presence of Ni on the surface can greatly promote 'OH adsorption. Consequently, ideal catalyst for HOR has been designed by regulating the distributions of Ni on ultrathin PtNi NWs. Detailed experimental investigations and DFT simulations further show that the surface Ni deposition on Pt NWs surface can regulate the adsorption towards 'OH, while the alloyed Ni with Pt NWs strongly varies the electronic properties of Pt and thus weakens the adsorption towards 'H. This work not only reveals the specific role of Ni for Pt on HOR, but also sheds new light on the surface modification of catalyst.

Acknowledgements

The authors thank the financial supports by the National Key R&D Program of China (No. 2020YFB1505802), the Ministry of Science and Technology of China (Nos. 2017YFA0208200, and 2016YFA0204100), the National Natural Science Foundation of China (Nos. 22025108, 22121001 and 51802206), Guangdong Provincial Natural Science Fund for Distinguished Young Scholars (No. 2021B1515020081), and Start-up Supports from Xiamen University and Guangzhou Key Laboratory of Low Dimensional Materials and Energy Storage Devices (No. 20195010002).

Electronic Supplementary Material: Supplementary material (extended figures, and tables) is available in the online version of this article at <https://doi.org/10.1007/s12274-022-4228-3>.

References

- [1] An, L. L.; Zhao, X.; Zhao, T. H.; Wang, D. L. Atomic-level insight into reasonable design of metal-based catalysts for hydrogen oxidation in alkaline electrolytes. *Energy Environ. Sci.* **2021**, *14*, 2620–2638.
- [2] Strmcnik, D.; Uchimura, M.; Wang, C.; Subbaraman, R.; Danilovic, N.; van der Vliet, D.; Paulikas, A. P.; Stamenkovic, V. R.; Markovic, N. M. Improving the hydrogen oxidation reaction rate by promotion of hydroxyl adsorption. *Nat. Chem.* **2013**, *5*, 300–306.
- [3] Song, J. D.; Jin, Y. Q.; Zhang, L.; Dong, P. Y.; Li, J. W.; Xie, F. Y.; Zhang, H.; Chen, J.; Jin, Y. S.; Meng, H. et al. Phase-separated Mo-Ni alloy for hydrogen oxidation and evolution reactions with high activity and enhanced stability. *Adv. Energy Mater.* **2021**, *11*, 2003511.
- [4] Zhou, Y. Y.; Xie, Z. Y.; Jiang, J. X.; Wang, J.; Song, X. Y.; He, Q.; Ding, W.; Wei, Z. D. Lattice-confined Ru clusters with high CO tolerance and activity for the hydrogen oxidation reaction. *Nat. Catal.* **2020**, *3*, 454–462.
- [5] Wang, H. S.; Abruña, H. D. Rh and Rh alloy nanoparticles as highly active H₂ oxidation catalysts for alkaline fuel cells. *ACS Catal.* **2019**, *9*, 5057–5062.
- [6] Zhao, Z. P.; Liu, H. Y.; Gao, W. P.; Xue, W.; Liu, Z. Y.; Huang, J.; Pan, X. Q.; Huang, Y. Surface-engineered PtNi-O nanostructure with record-high performance for electrocatalytic hydrogen evolution reaction. *J. Am. Chem. Soc.* **2018**, *140*, 9046–9050.
- [7] Alia, S. M.; Pivovar, B. S.; Yan, Y. S. Platinum-coated copper nanowires with high activity for hydrogen oxidation reaction in base. *J. Am. Chem. Soc.* **2013**, *135*, 13473–13478.
- [8] Shi, G.; Yano, H.; Tryk, D. A.; Iiyama, A.; Uchida, H. Highly active, CO-tolerant, and robust hydrogen anode catalysts: Pt-M (M = Fe, Co, Ni) alloys with stabilized Pt-skin layers. *ACS Catal.* **2017**, *7*, 267–274.
- [9] McCrum, I. T.; Koper, M. T. M. The role of adsorbed hydroxide in hydrogen evolution reaction kinetics on modified platinum. *Nat. Energy* **2020**, *5*, 891–899.
- [10] Ghoshal, S.; Jia, Q. Y.; Bates, M. K.; Li, J. K.; Xu, C. C.; Gath, K.; Yang, J.; Waldecker, J.; Che, H. Y.; Liang, W. T. et al. Tuning Nb–Pt interactions to facilitate fuel cell electrocatalysis. *ACS Catal.* **2017**, *7*, 4936–4946.
- [11] Shen, L. F.; Lu, B. A.; Qu, X. M.; Ye, J. Y.; Zhang, J. M.; Yin, S. H.; Wu, Q. H.; Wang, R. X.; Shen, S. Y.; Sheng, T. et al. Does the oxophilic effect serve the same role for hydrogen evolution/oxidation reaction in alkaline media? *Nano Energy* **2019**, *62*, 601–609.
- [12] Lu, S. Q.; Zhuang, Z. B. Investigating the influences of the adsorbed species on catalytic activity for hydrogen oxidation reaction in alkaline electrolyte. *J. Am. Chem. Soc.* **2017**, *139*, 5156–5163.
- [13] Kresse, G.; Hafner, J. *Ab initio* molecular dynamics for liquid metals. *Phys. Rev. B* **1993**, *47*, 558–561.
- [14] Kresse, G.; Hafner, J. *Ab initio* molecular-dynamics simulation of the liquid-metal-amorphous-semiconductor transition in germanium. *Phys. Rev. B* **1994**, *49*, 14251–14269.
- [15] Kresse, G.; Furthmüller, J. Efficient iterative schemes for *ab initio* total-energy calculations using a plane-wave basis set. *Phys. Rev. B* **1996**, *54*, 11169–11186.
- [16] Kresse, G.; Furthmüller, J. Efficiency of *ab-initio* total energy calculations for metals and semiconductors using a plane-wave basis set. *Comput. Mater. Sci.* **1996**, *6*, 15–50.
- [17] Perdew, J. P.; Chevary, J. A.; Vosko, S. H.; Jackson, K. A.; Pederson, M. R.; Singh, D. J.; Fiolhais, C. Atoms, molecules, solids, and surfaces: Applications of the generalized gradient approximation for exchange and correlation. *Phys. Rev. B* **1992**, *46*, 6671–6687.
- [18] Perdew, J. P.; Burke, K.; Ernzerhof, M. Generalized gradient approximation made simple. *Phys. Rev. Lett.* **1996**, *77*, 3865–3868.
- [19] Grimme, S.; Ehrlich, S.; Goerigk, L. Effect of the damping function in dispersion corrected density functional theory. *J. Comput. Chem.* **2011**, *32*, 1456–1465.
- [20] Mathew, K.; Sundararaman, R.; Letchworth-Weaver, K.; Arias, T. A.; Hennig, R. G. Implicit solvation model for density-functional study of nanocrystal surfaces and reaction pathways. *J. Chem. Phys.* **2014**, *140*, 084106.
- [21] Mathew, K.; Kolluru, V. S. C.; Mula, S.; Steinmann, S. N.; Hennig, R. G. Implicit self-consistent electrolyte model in plane-wave density-functional theory. *J. Chem. Phys.* **2019**, *151*, 234101.
- [22] Jin, Y.; Zhang, Z.; Yang, H.; Wang, P. T.; Shen, C. Q.; Cheng, T.; Huang, X. Q.; Shao, Q. Boosting hydrogen production with ultralow working voltage by selenium vacancy-enhanced ultrafine platinum-nickel nanowires. *SmartMat*, in press, <https://doi.org/10.1002/smm2.1083>.
- [23] Jiang, K. Z.; Zhao, D. D.; Guo, S. J.; Zhang, X.; Zhu, X.; Guo, J.; Lu, G.; Huang, X. Q. Efficient oxygen reduction catalysis by subnanometer Pt alloy nanowires. *Sci. Adv.* **2017**, *3*, e1601705.
- [24] Zhao, T. H.; Wang, G. J.; Gong, M. X.; Xiao, D. D.; Chen, Y.; Shen, T.; Lu, Y.; Zhang, J.; Xin, H. L.; Li, Q. et al. Self-optimized ligand effect in L1₂-PtPdFe intermetallic for efficient and stable alkaline hydrogen oxidation reaction. *ACS Catal.* **2020**, *10*, 15207–15216.
- [25] Zhu, Y. M.; Bu, L. Z.; Shao, Q.; Huang, X. Q. Subnanometer PtRh nanowire with alleviated poisoning effect and enhanced C–C bond cleavage for ethanol oxidation electrocatalysis. *ACS Catal.* **2019**, *9*, 6607–6612.
- [26] Zhao, T. H.; Hu, Y. C.; Gong, M. X.; Lin, R. Q.; Deng, S. F.; Lu, Y.; Liu, X. P.; Chen, Y.; Shen, T.; Hu, Y. Z. et al. Electronic structure

- and oxophilicity optimization of mono-layer Pt for efficient electrocatalysis. *Nano Energy* **2020**, *74*, 104877.
- [27] Scofield, M. E.; Zhou, Y. C.; Yue, S. Y.; Wang, L.; Su, D.; Tong, X.; Vukmirovic, M. B.; Adzic, R. R.; Wong, S. S. Role of chemical composition in the enhanced catalytic activity of Pt-based alloyed ultrathin nanowires for the hydrogen oxidation reaction under alkaline conditions. *ACS Catal.* **2016**, *6*, 3895–3908.
- [28] Wu, J.; Zhou, Y. J.; Nie, H. D.; Wei, K. Q.; Huang, H.; Liao, F.; Liu, Y.; Shao, M. W.; Kang, Z. H. Carbon dots regulate the interface electron transfer and catalytic kinetics of Pt-based alloys catalyst for highly efficient hydrogen oxidation. *J. Energy Chem.* **2022**, *66*, 61–67.
- [29] Chen, H. Q.; Wang, G. J.; Gao, T. Y.; Chen, Y. H.; Liao, H. G.; Guo, X. L.; Li, H. Y.; Liu, R. H.; Dou, M.; Nan, S. F. et al. Effect of atomic ordering transformation of PtNi nanoparticles on alkaline hydrogen evolution: Unexpected superior activity of the disordered phase. *J. Phys. Chem. C* **2020**, *124*, 5036–5045.
- [30] Zhu, S. Q.; Qin, X. P.; Xiao, F.; Yang, S. L.; Xu, Y.; Tan, Z.; Li, J. D.; Yan, J. W.; Chen, Q.; Chen, M. S. et al. The role of ruthenium in improving the kinetics of hydrogen oxidation and evolution reactions of platinum. *Nat. Catal.* **2021**, *4*, 711–718.
- [31] Chen, G. G.; Zhao, Y.; Fu, G.; Duchesne, P. N.; Gu, L.; Zheng, Y. P.; Weng, X. F.; Chen, M. S.; Zhang, P.; Pao, C. W. et al. Interfacial effects in iron-nickel hydroxide-platinum nanoparticles enhance catalytic oxidation. *Science* **2014**, *344*, 495–499.
- [32] Zhang, C.; Chen, B. H.; Mei, D. H.; Liang, X. The OH-driven synthesis of Pt-Ni nanocatalysts with atomic segregation for alkaline hydrogen evolution reaction. *J. Mater. Chem. A* **2019**, *7*, 5475–5481.
- [33] Gao, S.; Yang, X. X.; Liang, S.; Wang, Y. H.; Zang, H. Y.; Li, Y. G. One step synthesis of PtNi electrocatalyst for methanol oxidation. *Inorg. Chem. Commun.* **2019**, *106*, 104–110.
- [34] Yu, L.; Zhu, Q.; Song, S. W.; McElhenny, B.; Wang, D. Z.; Wu, C. Z.; Qin, Z. J.; Bao, J. M.; Yu, Y.; Chen, S. et al. Non-noble metal-nitride based electrocatalysts for high-performance alkaline seawater electrolysis. *Nat. Commun.* **2019**, *10*, 5106.
- [35] Duan, Y.; Yu, Z. Y.; Yang, L.; Zheng, L. R.; Zhang, C. T.; Yang, X. T.; Gao, F. Y.; Zhang, X. L.; Yu, X. X.; Liu, R. et al. Bimetallic nickel-molybdenum/tungsten nanoalloys for high-efficiency hydrogen oxidation catalysis in alkaline electrolytes. *Nat. Commun.* **2020**, *11*, 4789.
- [36] Zhuang, Z. B.; Giles, S. A.; Zheng, J.; Jenness, G. R.; Caratzoulas, S.; Vlachos, D. G.; Yan, Y. S. Nickel supported on nitrogen-doped carbon nanotubes as hydrogen oxidation reaction catalyst in alkaline electrolyte. *Nat. Commun.* **2016**, *7*, 10141.
- [37] Mao, J. J.; He, C. T.; Pei, J. J.; Liu, Y.; Li, J.; Chen, W. X.; He, D. S.; Wang, D. S.; Li, Y. D. Isolated Ni atoms dispersed on Ru nanosheets: High-performance electrocatalysts toward hydrogen oxidation reaction. *Nano Lett.* **2020**, *20*, 3442–3448.
- [38] Xue, Y. R.; Shi, L.; Liu, X. R.; Fang, J. J.; Wang, X. D.; Setzler, B. P.; Zhu, W.; Yan, Y. S.; Zhuang, Z. B. A highly-active, stable and low-cost platinum-free anode catalyst based on RuNi for hydroxide exchange membrane fuel cells. *Nat. Commun.* **2020**, *11*, 5651.
- [39] Qin, S.; Duan, Y.; Zhang, X. L.; Zheng, L. R.; Gao, F. Y.; Yang, P. P.; Niu, Z. Z.; Liu, R.; Yang, Y.; Zheng, X. S. et al. Ternary nickel-tungsten-copper alloy rivals platinum for catalyzing alkaline hydrogen oxidation. *Nat. Commun.* **2021**, *12*, 2686.
- [40] Gao, L.; Li, X. X.; Yao, Z. Y.; Bai, H. J.; Lu, Y. F.; Ma, C.; Lu, S. F.; Peng, Z. M.; Yang, J. L.; Pan, A. L. et al. Unconventional p-d hybridization interaction in PtGa ultrathin nanowires boosts oxygen reduction electrocatalysis. *J. Am. Chem. Soc.* **2019**, *141*, 18083–18090.
- [41] Yakovina, O. A.; Lisitsyn, A. S. Probing the H₂-induced restructuring of Pt nanoclusters by H₂-TPD. *Langmuir* **2016**, *32*, 12013–12021.